J. Fluid Mech. (2008), *vol.* 612, *pp.* 237–260. © 2008 Cambridge University Press
doi:10.1017/S0022112008002966 Printed in the United Kingdom

The stability of the variable-density Kelvin–Helmholtz billow

JÉRÔME FONTANE AND LAURENT JOLY
Université de Toulouse, ISAE, 10 Av. Édouard Belin, 31055 Toulouse, France

(Received 12 September 2007 and in revised form 10 June 2008)

We perform a three-dimensional stability analysis of the Kelvin–Helmholtz (KH) billow, developing in a shear layer between two fluids with different density. We begin with two-dimensional simulations of the temporally evolving mixing layer, yielding the unsteady base flow fields. The Reynolds number is 1500 while the Schmidt and Froude numbers are infinite. Then exponentially unstable modes are extracted from a linear stability analysis performed at the saturation of the primary mode kinetic energy. The spectrum of the least stable modes exhibits two main classes. The first class comprises three-dimensional core-centred and braid-centred modes already present in the homogeneous case. The baroclinic vorticity concentration in the braid lying on the light side of the KH billow turns the flow into a sharp vorticity ridge holding high shear levels. The hyperbolic modes benefit from the enhanced level of shear in the braid whereas elliptic modes remain quite insensitive to the modifications of the base flow. In the second class, we found typical two-dimensional modes resulting from a shear instability of the curved vorticity-enhanced braid. For a density contrast of 0.5, the wavelength of the two-dimensional instability is about ten times shorter than that of the primary wave. Its amplification rate competes well against those of the hyperbolic three-dimensional modes. The vorticity-enhanced braid thus becomes the preferred location for the development of secondary instabilities. This stands as the key feature of the transition of the variable-density mixing layer. We carry out a fully resolved numerical continuation of the nonlinear development of the two-dimensional braid-mode. Secondary roll-ups due to a small-scale Kelvin–Helmholtz mechanism are promoted by the underlying strain field and develop rapidly in the compression part of the braid. Originally analysed by Reinoud *et al.* (*Phys. Fluids*, vol. 12, 2000, p. 2489) from two-dimensional non-viscous numerical simulations, this instability is shown to substantially increase the mixing.

1. Introduction

The interest in turbulent mixing layers stems from their recurrence in geophysical and industrial flows. They often develop with mass variations resulting from thermal mixing, compressibility effects or the mingling of fluids of different densities. This motivated the early experimental work of Brown & Roshko (1974) who investigated the density effect on the shear-layer development. Mass inhomogeneities introduce inertia differentials responsible for the modification of the flow. More precisely, the baroclinic torque alters the vorticity dynamics where the density gradient and the pressure gradient are misaligned. In the inviscid limit, the baroclinic torque is simply proportional to the vector product between the density gradient and the acceleration field. In stratified geophysical flows, gravity introduces a fixed external acceleration and gives rise to a well-known vorticity source. This gravitational baroclinic vorticity production has been shown to alter significantly the stability characteristics of a stratified shear layer under the Boussinesq approximation. In high-Froude-number flows, the acceleration comes only from the variation of the fluid velocity along the particle path. We label the corresponding vorticity source the inertial baroclinic torque. We focus here on its consequences on the stability characteristics of the variable-density mixing layer in the limit of infinite Froude number and zero Mach number.

In homogeneous mixing layers, previous works contributed to the well-accepted standard route to three-dimensionality. It relies on both streamwise vortices lying in the braid region between two consecutive Kelvin–Helmholtz (KH) billows and core undulation of the primary rollers (see Jimenez 1983; Corcos & Lin 1984; Bernal & Roshko 1986, Lasheras, Cho & Maxworthy 1986; Ashurst & Meiburg 1988; Lasheras & Choi 1988; Nygaard & Glezer 1990). Core-centred or elliptic modes – referred to as the ‘translative’ instability of Pierrehumbert & Widnall (1982) – as well as braid-centred or hyperbolic modes contribute to the development of these three-dimensional motions (Metcalfe *et al.* 1987; Klaassen & Peltier 1991; Rogers & Moser 1992). Both kinds of instabilities essentially derive their energy from shear conversion as shown by Klaassen & Peltier (1991 – hereinafter referred to as KP91).

In the stratified mixing layer, the selection of three-dimensional secondary modes is modified. The stability analysis of Klaassen & Peltier (1985) pointed out that convective instabilities related to the Rayleigh–Taylor mechanism appear in the superadiabatic regions where stratification is locally reversed during the rolling of the KH wave. For a large enough Richardson number, KP91 demonstrated that these modes essentially derive their growth from potential energy conversion. These authors also predicted that convective modes dominate the three-dimensional transition stage of the flow since they possess the maximum linear growth rate. Schowalter, Van Atta & Lasheras (1994) confirmed this point experimentally by visualizing streamwise baroclinically generated vortices at the unstable density interface. These buoyancy-induced longitudinal structures are enhanced by the initial development of the streamwise ribs also occurring in the homogeneous case. Even for Richardson numbers as small as 0.03, they dominate the three-dimensional structure as the flow evolves downstream. Most of these results were retrieved by Cortesi, Yadigaroglu & Banerjee (1998) with direct numerical simulations. Besides these three-dimensional modes, a two-dimensional Kelvin–Helmholtz instability can emerge at the braid saddle point, as first observed by Staquet (1995). This secondary mode was not detected in KP91 stability analysis because of the small value of their Reynolds number. As demonstrated by Smyth (2003), the onset of this Kelvin–Helmholtz mode is promoted by high Reynolds numbers and, to a lesser extent, by high Prandtl numbers.

By contrast, the high-Froude-number variable-density mixing layer where the inertial baroclinic torque is active, has been much less well documented. However, it is an example of high-Reynolds-number mixing between gases of different densities with applications in combustion. As its homogeneous counterpart, the variable-density shear layer is sensitive to the Kelvin–Helmholtz instability. The roll-up of the vorticity sheet exhibits specific features due to baroclinic vorticity redistribution. We term the resulting large-scale structures the variable-density Kelvin–Helmholtz (VDKH) billows. Soteriou & Ghoniem (1995) illustrated the symmetry breaking of the streamline pattern and detailed the density-induced biases on the entrainment and the convection velocity. They considered the baroclinic vorticity production as a superimposed counter-rotative dipole centred on the braid saddle point. This simple model yields the essential modifications due to the density contrast. As demonstrated by Reinaud, Joly & Chassaing (2000), baroclinic vorticity generation on the light side of the VDKH billow triggers a two-dimensional secondary instability providing a two-dimensional route to turbulence. This shear instability of the vorticity enhanced braid results from the strain–vorticity competition addressed theoretically by Dritschel *et al.* (1991) in the homogeneous case.

Few studies so far have dealt with the three-dimensional evolution of the inhomogeneous shear layer. Using a three-dimensional inviscid vortex method, Knio & Ghoniem (1992) gave a first description of this transition stage for a density ratio of 2. They observed the symmetry breaking of the flow induced by the baroclinic torque which unevenly affects the development of the streamwise ribs. The vorticity of the longitudinal vortices lying on the low-density (resp. high-density) side is intensified (resp. weakened). Joly, Reinaud & Chassaing (2001) performed viscous simulations at a density ratio of 3 in which the baroclinic torque contributed significantly to the dynamics of the streamwise vortices. Both studies suffered from a lack of *a priori* knowledge of the most amplified three-dimensional mode to seed their nonlinear simulations. As mentioned by the previous authors, the three-dimensional linear stability analysis of such a flow has not been treated so far. In this paper, we determine how secondary modes are modified under the influence of the inertial baroclinic torque.

In order to carry out this linear stability analysis, two major difficulties have to be considered. First, there is no analytical solution for the velocity and density fields of the VDKH nonlinear wave. Secondly, the temporal stability study requires a steady basic state. Klaassen & Peltier (1985, 1989, 1991) overcame these two obstacles when considering the three-dimensional secondary instabilities of the stratified mixing layer. They chose first to obtain the two-dimensional base flow fields from a numerical simulation of the temporally evolving shear layer. They then based the stability analysis on a quasi-steady approach, assuming that three-dimensional disturbances grow on a time scale shorter than the two-dimensional primary rollers. They performed the stability calculations throughout the development of the KH wave and validate *a posteriori* the unstable modes in agreement with the quasi-static assumption. Unstable modes, persistent on a long-enough time period, are considered likely to grow in the stratified mixing layer. We adopt the same methodology in the present case.

The paper is organized as follows. The numerical simulation leading to the generation of the nonlinear VDKH wave is briefly presented in § 2. We also describe the characteristics of the base flow relevant to the development of three-dimensional modes. We derive the equations for the three-dimensional linear stability analysis in § 3. The numerical method to solve the eigen-problem is detailed and validated in the same section. The results of the three-dimensional stability analysis of the inhomogeneous mixing layer are detailed in the next section. At the saturation time of the primary wave, we obtain the spectra of unstable modes for increasing density contrasts. Among all the instabilities inventoried, we retrieve the two-dimensional Kelvin–Helmholtz-type instability found by Reinaud *et al.* (2000). Seeding the base flow at saturation time with this two-dimensional mode, we explore the nonlinear development of the two-dimensional baroclinic instability in § 5. Our conclusions and perspectives are given in § 6.

2. The variable-density Kelvin–Helmholtz wave

2.1. *Governing equations*

In the context of linear stability analysis, viscous terms prevent small-scale physically irrelevant instabilities from being amplified, as stressed by Klaassen & Peltier (1985, 1991) or Mayer & Powell (1992). Hence we chose to establish the base two-dimensional flow maps based on a viscous model and to derive the stability analysis accordingly. The objective of the paper is to find out the upper bound of density effects on secondary instabilities of the VDKH billows. In order to obtain the most biased response, we do not retain mass diffusion or equivalently assume an infinite Schmidt number. This choice is supported by the work of Smyth (2003) showing that the development of a two-dimensional secondary mode in the stratified mixing layer is enhanced when both Prandtl and Reynolds numbers are increased. In absence of mass diffusion, the density gradients remain steep, leading to the highest possible intensity of the baroclinic torque. Besides, this assumption induces a divergence-free flow (see Joseph 1990). As will be discussed in § 3, this avoids tedious algebra for the derivation of the stability equations. Under the infinite-Schmidt-number assumption, the governing equations read

$$\nabla\cdot\boldsymbol{u} = 0, \tag{2.1a}$$

$$\rho \mathrm{D}_t \boldsymbol{u} = -\nabla p + \frac{1}{Re}\Delta\boldsymbol{u}, \tag{2.1b}$$

$$\mathrm{D}_t \rho = 0, \tag{2.1c}$$

where $\mathrm{D}_t = \partial_t + \boldsymbol{u}\cdot\nabla$ stands for the material derivative. We take u_0 half the velocity difference across the shear layer, $2l_0$ the shear-layer depth and $\rho_0 = (\rho_{upper} + \rho_{lower})/2$ the mean density as characteristic velocity, length and density scales. The resulting characteristic time scale is $t_0 = l_0/u_0$. The Reynolds number, defined by $Re = (u_0 l_0 \rho_0)/\mu$, is set to 1500, well in the range of similar studies Staquet (1995); Smyth (2003) devoted to secondary modes biased or triggered by modifications of the base flow due to density variations. The dynamic viscosity μ is kept constant, which is a fair approximation for the air–helium couple (see Fontane 2005). A relevant measure of the inertia effects is the density contrast $C_\rho = \Delta\rho/2\rho_0$ where $\Delta\rho = \rho_{upper} - \rho_{lower}$ is the density difference across the shear layer. We address buoyancy-free flows where the Froude number, defined by $Fr = u_0/\sqrt{g l_0 C_\rho}$ with g the acceleration due to gravity, is infinite.

2.2. *Initial conditions*

The x-axis is in the longitudinal direction and the y-axis in the crosswise direction. The spanwise dimension along the z-axis will serve for the stability analysis. Co-gradient and counter-gradient variable-density mixing layers correspond to shear flows where the crosswise density and velocity gradients are, respectively, of the same or of opposite signs. In the frame of the temporal approximation, these two situations are equivalent since the Galilean transformation $(x, y) \rightarrow (-x, -y)$ turns one situation into the other. We arbitrarily choose to place the denser fluid in the upper part of the flow. The normalized profiles of velocity $\boldsymbol{u} = (u^\dagger, 0)$ and density $\rho^\dagger$ that determine the initial variable-density parallel shear flow are:

$$u^\dagger(y) = \tanh\left(y - \tfrac{1}{2}H\right), \tag{2.2}$$

$$\rho^\dagger(y) = 1 + C_\rho \tanh\left(y - \tfrac{1}{2}H\right). \tag{2.3}$$

We carry out a classical inviscid temporal linear stability analysis on this parallel flow with growing density contrast from 0 to 0.5. Hence we search for modal solutions for the crosswise velocity perturbation $\hat{v} = \tilde{v}(y)\exp(\alpha x - \alpha c t)$ of the Rayleigh equation. Generalized to the case with density variations across the layer, this equation is

$$[(u^\dagger - c)(\rho^\dagger(\mathscr{D}^2 - \alpha^2) + \rho^{\dagger\prime}\mathscr{D}) - (\rho^\dagger u^{\dagger\prime})^\prime]\,\tilde{v} = 0, \tag{2.4}$$

C_ρ	0	0.1	0.2	0.3	0.4	0.5
α	0.444	0.447	0.453	0.464	0.479	0.498
αc_i	0.189	0.190	0.190	0.191	0.191	0.192
c_r	0	0.059	0.117	0.174	0.229	0.281

TABLE 1. Characteristics of the most unstable mode of the temporally evolving variable-density mixing layer. Wavenumber α, amplification rate αc_i and phase velocity c_r.

where $\mathscr{D}$ and prime stand, respectively, for the crosswise differentiation of the perturbation and the base flow fields, α is the streamwise wavenumber and c the complex phase velocity. The density perturbation in the form $\hat{\rho} = \tilde{\rho}(y)\exp(\alpha x - \alpha c t)$ is deduced from the crosswise velocity by the linearized continuity equation,

$$[\mathrm{i}\alpha(u^\dagger - c)]\,\tilde{\rho} = -\rho^{\dagger\prime}\tilde{v}. \tag{2.5}$$

Table 1 gives the characteristics of the most unstable Kelvin–Helmholtz mode. It can be seen that the amplification rate is quite insensitive to the density contrast. The wavenumber of the most amplified mode slightly increases with C_ρ whereas the phase velocity grows almost linearly in the direction of the upper high-density flow. We stress that the structure of the most unstable mode also changes with the density contrast as detailed in Joly (2002). We perturb the initially parallel flow with the most unstable mode and we set the perturbation amplitude such that the enstrophy of the perturbation is 4 % of the enstrophy of the shear layer over a period.

2.3. *The VDKH billows*

Equations (2.1*a*)–(2.1*c*) are advanced in time from the initial conditions by a two-dimensional dealiased pseudospectral method described in Joly, Fontane & Chassaing (2005) and Joly & Reinaud (2007). The two-dimensional velocity components (U, V) and the density R are calculated on the domain $[0, \lambda_x] \times [0, H]$, with a periodic longitudinal boundary condition and a free-slip boundary condition in the crosswise direction, i.e.

$$\partial_y U = 0, \quad V = 0, \quad \partial_y R = 0, \qquad y = 0,\ H. \tag{2.6}$$

Such free-slip boundary conditions are implemented in the pseudospectral frame based on crosswise symmetries or antisymmetries on a $2H$-wide period with the respective use of cosine- and sine-transforms (see Staquet 1995). The width of the domain is set to $H = \lambda_x$ such that the slip-free walls do not strongly affect the nonlinear development of the flow. The infinite-Schmidt-number condition demands that the density field be resolved down to the smallest scales. For this purpose, we estimate the order of magnitude of the relative density gradient by

$$\frac{1}{R}|\nabla R| \sim \frac{C_\rho}{\eta_\rho}, \tag{2.7}$$

where η_ρ is a characteristic length scale of the density gradient. As in Joly *et al.* (2005), a procedure of growing spectral radius is adopted which corresponds to a mesh refinement in the physical space. The need for increased spatial resolution is felt when the condition $\Delta < \min(\eta_\rho)/3$ is violated. Here Δ denotes the smallest length scale properly resolved by the dealiased pseudospectral approach, i.e. the nonlinear terms are computed in the physical space on a grid with size $\Delta_{nl} = 2\Delta/3$. The refinement constraint is illustrated in figure 1(*a*) for the most density contrasted simulation and compared to the smoother case with mass diffusion and unit Schmidt

C_ρ	0	0.1	0.2	0.3	0.4	0.5
ω_{max}	0	0.078	0.461	0.838	1.216	1.614
ω_{min}	−0.501	−0.705	−1.090	−1.448	−1.765	−2.041
$\bar{\sigma}_{KH}$	-2.10^{-3}	3.10^{-3}	3.10^{-3}	3.10^{-3}	2.10^{-3}	2.10^{-4}
$N_x \times N_y$	340^2	2054^2	2688^2	2688^2	3584^2	4106^2

TABLE 2. Characteristics of the two-dimensional VDKH billows at saturation time $t = 26$. Maximum and minimum vorticity on the period ω_{max} and ω_{min}, mean growth rate around saturation time $\bar{\sigma}_{KH} = (1/4)\int_{24}^{28} \sigma_{\mathrm{KH}} \mathrm{d}t$ with σ_{KH} defined by (3.6) and grid size based on $\varDelta$.

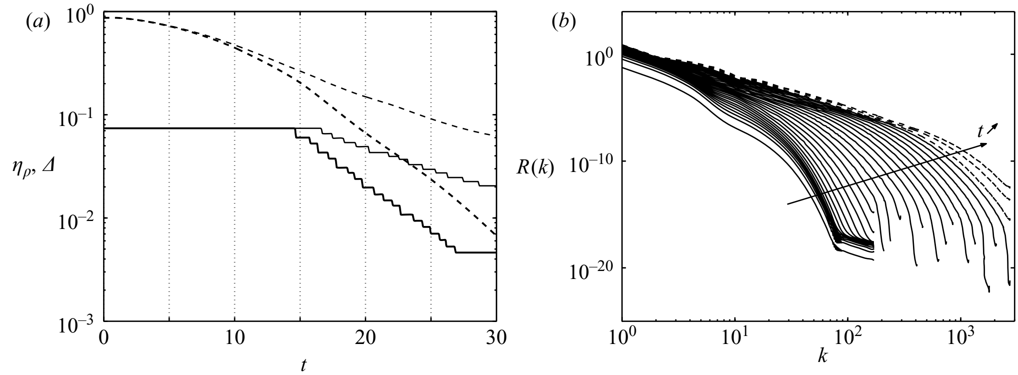

FIGURE 1. (a) Characteristic length scale of the density gradient η_ρ (dashed lines) and the smallest length scale properly resolved by the dealiased pseudospectral approach $\varDelta$ (solid lines) for $C_\rho = 0.5$. Thick lines correspond to an infinite Schmidt number, $Sc = \infty$, and thin lines to $Sc = 1$. (b) Time spreading of the density variance spectra for $C_\rho = 0.5$ and $Sc = \infty$. Dashed spectra correspond to $t = 28, 29$ and 30 when the constraint in spatial resolution, $\varDelta < \min(\eta_\rho)/3$, is released.

number. The spatial resolution of the exponentially decreasing density length scale is paid for by a corresponding growth of the grid size, as detailed in table 2 for $t = 26.0$. This is accompanied by a corresponding decrease of the time step owing to the stability constraint of the time-advancement scheme. We afforded the associated increase in computational cost up to a maximum grid size of 5376^2 in terms of $\varDelta$. This limit is seen to be reached at $t = 27.5$ when $C_\rho = 0.5$, hence the plateau at the tail of the thick curve in figure 1(a). It is reached later for less density contrasted mixing layers owing to the lower stretching rate of the density braid associated with lower growth rates of the primary mode (see table 1). The self-adaptive refinement procedure allows the proper representation of a density variance spectrum spreading towards larger wavenumbers without small-scale dissipation (see figure 1b). Slight small-scale variance accumulation is observed on the three last spectra corresponding to $t = 28, 29$ and 30, i.e. after the resolution constraint is released. The criterion $\varDelta < \min(\eta_\rho)/3$ is thus demonstrated to ensure the resolution of a pure transport equation for the density in our numerical frame at least before $t = 27.5$. Close inspection of the density field up to $t = 30$, where still $\min(\eta_\rho)/\Delta = 1.45$, does not exhibit any oscillation or overshoots and the base flow fields can be confidently used for the purpose of stability analysis.

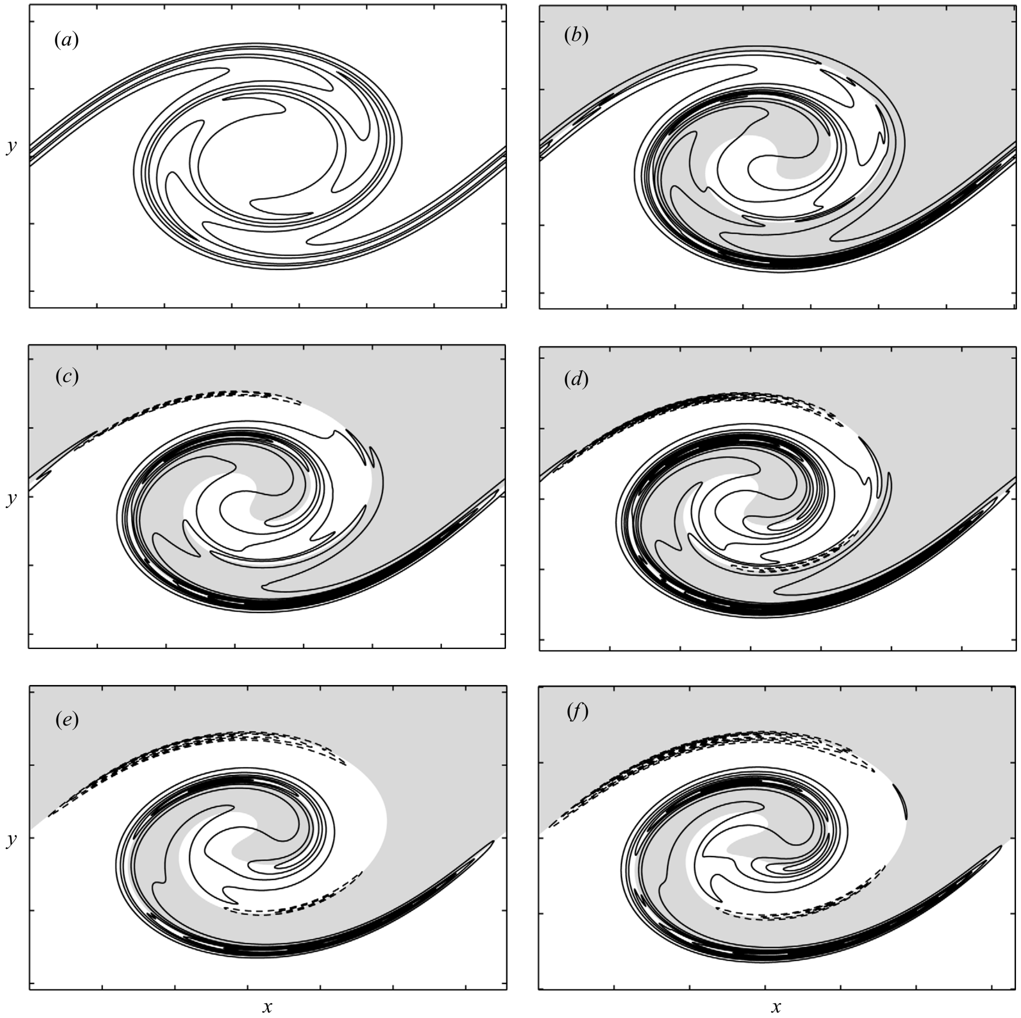

FIGURE 2. Vorticity contours at $t = 26$ of the temporally evolving mixing layer with increasing density contrasts (*a*) $C_\rho = 0$, (*b*) $C_\rho = 0.1$, (*c*) $C_\rho = 0.2$, (*d*) $C_\rho = 0.3$, (*e*) $C_\rho = 0.4$ and (*f*) $C_\rho = 0.5$. The vorticity increment between contours is $1/6t_0$ in (*a*) and (*b*), $1/4t_0$ in (*c*) and (*d*), and $1/2t_0$ in (*e*) and (*f*). Positive contours are drawn with dashed lines. The grey-shaded region corresponds to the domain where the density is higher than ρ_0. Tick marks along x and y axes are separated by the initial vorticity thickness $\delta_\omega^0 = 2l_0$.

Figure 2 displays the vorticity field at $t = 26$ near the saturation time of the primary mode. Inertia effects yield a growing departure from the symmetric Kelvin–Helmholtz billow of the homogeneous mixing layer. The baroclinic source–sink system advocated by Soteriou & Ghoniem (1995) and Reinaud *et al.* (2000) triggers the asymmetry of the vorticity field together with a concentration of the circulation on thinning vorticity sheets of opposite signs. The vorticity is redistributed in favour of the half of the braid lying on the light side. The other half is vorticity depleted in a first stage and then exhibits vorticity of opposite sign. For the sake of clarity, the contour increment is increased with growing density contrast. Though similar in structure, the level of negative vorticity on the favoured side of the braid dramatically increases with growing density contrast as reported in table 2. The spatial organization of the flow in sharp vorticity ridges, holding high shear rates, discard any three-dimensional stability analysis based on the Stuart vortex model. Following the conclusion of KP91, the shear instability being the fundamental mechanism for the onset of three-dimensional motions, we expect three-dimensional instabilities to move towards the regions of shear production. Our position then contrasts with the analysis by O'Reilly & Pullin (2003). These authors address the compressibility effects on the stability of the compressible Stuart vortices taken as a representative model of the high-speed homogeneous mixing layer. We deal with incompressible mixing of inhomogeneous flows where the structural difference with the homogeneous base field comes from baroclinic vorticity sources. No stationary analytical model may approach the actual two-dimensional nonlinear wave in this case. Thus, we resort to a quasi-steady approach to probe the sensitivity of the VDKH billows against three-dimensional modes. This is the objective of the next section.

3. Formulation of the problem

3.1. *The method for the stability analysis*

We linearize (2.1*a*)–(2.1*c*) by expanding the velocity, density and pressure fields as

$$\boldsymbol{u}(x, y, z, t) = \boldsymbol{U}(x, y) + \hat{\boldsymbol{u}}(x, y, z, t), \tag{3.1a}$$

$$\rho(x, y, z, t) = R(x, y) + \hat{\rho}(x, y, z, t), \tag{3.1b}$$

$$p(x, y, z, t) = P(x, y) + \hat{p}(x, y, z, t), \tag{3.1c}$$

where $\boldsymbol{U} = (U, V)$, P and R represent the two-dimensional base-flow fields provided by the VDKH billow calculations of §2.3, and $\hat{\boldsymbol{u}} = (\hat{u}, \hat{v}, \hat{w})$, $\hat{p}$ and $\hat{\rho}$ the three-dimensional perturbations. We obtain:

$$\mathrm{D}_t\hat{\rho} + \hat{\boldsymbol{u}}\cdot\nabla R = 0 = \nabla\hat{\boldsymbol{u}}, \tag{3.2}$$

$$R\mathrm{D}_t\hat{\boldsymbol{u}} + R\hat{\boldsymbol{u}}\cdot\nabla\boldsymbol{U} + \hat{\rho}\boldsymbol{U}\cdot\nabla\boldsymbol{U} = -\nabla\hat{p} + \frac{1}{Re}\Delta\hat{\boldsymbol{u}}. \tag{3.3}$$

The boundary conditions at $y = 0$ and $y = H$ are

$$\hat{v} = 0, \quad \partial_y\hat{u} = \partial_y\hat{w} = 0, \quad \hat{\rho} = 0, \quad \partial_y\hat{p} = \frac{1}{Re}\partial_y^2\hat{v}. \tag{3.4}$$

A Fourier expansion is assumed in the z-direction as no coefficient of the linear problem involves a z-dependence. Furthermore, the base-flow being x-periodic, we apply the Floquet theory as in Klaassen & Peltier (1985, 1989, 1991), Leblanc & Cambon (1998) and O'Reilly & Pullin (2003). Hence perturbations have a modal representation of the form:

$$[\hat{u}, \hat{v}, \hat{w}, \hat{p}, \hat{\rho}]\,(x, y, z, t) = [\tilde{u}, \tilde{v}, \tilde{w}, \tilde{p}, \tilde{\rho}]\,(x, y)\mathrm{e}^{\mathrm{i}(\mu x + kz) + \sigma t}, \tag{3.5}$$

where k is the real spanwise wavenumber, μ is the real Floquet exponent and $\sigma = \sigma_r + \mathrm{i}\omega$ is the complex frequency. We denote by σ_r the temporal growth rate and ω the temporal frequency of the perturbation. Following Klaassen & Peltier (1985, 1989, 1991), the exponential time-dependence is justified with a quasi-steady approach. We assume that the flow evolves on two separate time scales, the slower being associated with the VDKH billows and the faster being associated with secondary three-dimensional instabilities. Thus, it must be subjected to an *a posteriori* validation based on the comparison between temporal growth rates. Among the amplified modes, we retain those with a temporal growth rate σ_r large compared to the growth rate of the VDKH wave, i.e.

$$\sigma_r \gg \sigma_{\mathrm{KH}} = \frac{1}{2K}\frac{\mathrm{d}K}{\mathrm{d}t}, \tag{3.6}$$

where K is the kinetic energy of the nonlinear VDKH billows defined in KP91. Substituting the perturbations of the form (3.5) into the linearized equations (3.2) and (3.3) yields:

$$\sigma R\tilde{u} + RU\tilde{\partial}_x\tilde{u} + RV\partial_y\tilde{u} + RU_x\tilde{u} + RU_y\tilde{v} + (UU_x + VU_y)\tilde{\rho} = -\tilde{\partial}_x\tilde{p} + \frac{1}{Re}\tilde{\Delta}\tilde{u}, \tag{3.7a}$$

$$\sigma R\tilde{v} + RU\tilde{\partial}_x\tilde{v} + RV\partial_y\tilde{v} + RV_x\tilde{u} + RV_y\tilde{v} + (UV_x + VV_y)\tilde{\rho} = -\partial_y\tilde{p} + \frac{1}{Re}\tilde{\Delta}\tilde{v}, \tag{3.7b}$$

$$\sigma R\tilde{w} + RU\tilde{\partial}_x\tilde{w} + RV\partial_y\tilde{w} = -\mathrm{i}k\tilde{p} + \frac{1}{Re}\tilde{\Delta}\tilde{w}, \tag{3.7c}$$

$$\sigma\tilde{\rho} + U\tilde{\partial}_x\tilde{\rho} + V\partial_y\tilde{\rho} + R_x\tilde{u} + R_y\tilde{v} = 0, \tag{3.7d}$$

$$\tilde{\partial}_x\tilde{u} + \partial_y\tilde{v} + \mathrm{i}k\tilde{w} = 0, \tag{3.7e}$$

where $\tilde{\partial}_x \equiv (\mathrm{i}\mu + \partial_x)$ and the differential operator

$$\tilde{\Delta} \equiv \tilde{\partial}_x^2 + \partial_{yy} - k^2. \tag{3.8}$$

In order to eliminate the pressure terms, the Poisson equation is derived by taking the divergence of the momentum equation (3.2):

$$\begin{aligned}\tilde{\Delta}\tilde{p} = {} & -2R[U_x\tilde{\partial}_x\tilde{u} + V_x\partial_y\tilde{u} + U_y\tilde{\partial}_x\tilde{v} + V_y\partial_y\tilde{v}] \\ & - R_x[\sigma\tilde{u} + U\tilde{\partial}_x\tilde{u} + V\partial_y\tilde{u} + U_x\tilde{u} + U_y\tilde{v}] \\ & - R_y[\sigma\tilde{v} + U\tilde{\partial}_x\tilde{v} + V\partial_y\tilde{v} + V_x\tilde{u} + V_y\tilde{v}] \\ & - (UU_x + VU_y)\tilde{\partial}_x\tilde{\rho} - (UV_x + VV_y)\partial_y\tilde{\rho} \\ & - \left[U_x^2 + 2U_yV_x + V_y^2\right]\tilde{\rho}\,. \end{aligned} \tag{3.9}$$

The symmetries outlined by Klaassen & Peltier (1985, 1989, 1991) in the stratified case still hold for the system (3.7*a*)–(3.7*e*) and the search for unstable modes is restricted to $0 \leqslant \mu \leqslant 1/2$ and $k \geqslant 0$. The eigenvalues σ are also expected to be real or to appear in complex-conjugate pairs. Because of the bounded nature of the base fields in the crosswise direction, we implement a Fourier–Galerkin method similar to that developed by KP91, to carry out the stability analysis of the VDKH waves. The perturbations are expanded on the following Galerkin basis according to the boundary conditions (3.4):

$$[\tilde{u}, \tilde{w}, \tilde{p}]\,(x, y) = \sum_{m=-\infty}^{\infty}\sum_{n=0}^{\infty}[u_{nm}, w_{nm}, p_{nm}]\,\mathrm{e}^{\mathrm{i}mx}\cos\left(\frac{n\pi y}{H}\right), \tag{3.10}$$

$$[\tilde{v}, \tilde{\rho}]\,(x, y) = \sum_{m=-\infty}^{\infty}\sum_{n=1}^{\infty}[v_{nm}, \rho_{nm}]\,\mathrm{e}^{\mathrm{i}mx}\sin\left(\frac{n\pi y}{H}\right). \tag{3.11}$$

We subtitute (3.10) and (3.11) into the system (3.7*a*)–(3.7*e*) and (3.9). The inner product of each equation with the complex conjugate of the appropriate basis function yields the following eigensystem :

$$B_q p_{pq} = \sigma J^{(1)}_{npmq}u_{nm} + J^{(2)}_{npmq}u_{nm} + J^{(3)}_{npmq}v_{nm} + J^{(4)}_{npmq}\rho_{nm}, \tag{3.12a}$$

$$D_p p_{pq} = \sigma J^{(5)}_{npmq}v_{nm} + J^{(6)}_{npmq}u_{nm} + J^{(7)}_{npmq}v_{nm} + J^{(8)}_{npmq}\rho_{nm}, \tag{3.12b}$$

$$\mathrm{i}kp_{pq} = \sigma J^{(1)}_{npmq} w_{nm} + J^{(9)}_{npmq} w_{nm}, \tag{3.12c}$$

$$\sigma \rho_{pq} = J^{(10)}_{npmq} \rho_{nm} + J^{(11)}_{npmq} u_{nm} + J^{(12)}_{npmq} v_{nm}, \tag{3.12d}$$

$$0 = \mathrm{i}B_q u_{pq} + D_p v_{pq} + \mathrm{i}k w_{pq}, \tag{3.12e}$$

$$A_{pq} p_{pq} = \left(\sigma J^{(13)}_{npmq} + J^{(14)}_{npmq}\right) u_{nm} + \left(\sigma J^{(15)}_{npmq} + J^{(16)}_{npmq}\right) v_{nm} + J^{(17)}_{npmq} \rho_{nm}, \tag{3.12f}$$

where

$$B_m = \mu + m, \quad D_n = \left(\frac{n\pi}{H}\right), \quad A_{nm} = B_m^2 + D_n^2 + k^2, \tag{3.13}$$

and summation is implied over repeated indices. The interaction matrices $J^{(i)}_{npmq}$ which are not explicated here for clarity consist of inner products between basis functions and base-flow fields, see Fontane (2005) for their detailed expressions. Following the discussion of Klaassen & Peltier (1985), the eigensystem can be reduced to a closed set of three equations by eliminating the pressure in (3.12*a*)–(3.12*c*) with (3.12*f*):

$$\sigma I^{(1)}_{npmq} u_{nm} = \left(I^{(2)}_{npmq} + \frac{A_{nm}}{Re}\right) u_{nm} + I^{(3)}_{npmq} v_{nm} + I^{(4)}_{npmq} \rho_{nm}, \tag{3.14a}$$

$$\sigma I^{(5)}_{npmq} v_{nm} = \left(I^{(6)}_{npmq} + \frac{A_{nm}}{Re}\right) u_{nm} + I^{(7)}_{npmq} v_{nm} + I^{(8)}_{npmq} \rho_{nm}, \tag{3.14b}$$

$$\sigma \rho_{pq} = I^{(9)}_{npmq} \rho_{nm} + I^{(10)}_{npmq} u_{nm} + I^{(11)}_{npmq} v_{nm}. \tag{3.14c}$$

Truncating the expansions (3.10) and (3.11) at some finite level N, the system (3.14*b*)–(3.14*c*) is finally cast into a matrix-eigenvalue problem of the form $Ax = \sigma Bx$ with $x = [u_{nm}, v_{nm}, \rho_{nm}]$. The truncation scheme adopted is $2|m + \mu| + n \leqslant N$. The eigenvalue problem is solved using LAPACK routines from the Intel MKL library. The characteristics of the unstable modes depend mainly on the truncation level N, and to a lesser extent on the vertical domain length H. The size M of the generalized eigenvalue problem is $O(N^2)$. Its solution is based on the so-called QZ-algorithm whose cost grows as M^2. This is also the cost of the summations resulting in the interaction matrices I_{npmq}. For all calculations presented here, N has been fixed to 55. In the homogeneous case, we checked that this is large enough to reach a 1 % convergence of the amplification rate and phase velocity at least for the most-amplified branches presented hereinafter. KP91 used truncation levels of $N = 35$ (resp. $N = 27$) for the stability analysis of the homogeneous (resp. stratified) mixing layer. The sensitivity of the results to the vertical extent of the domain H has been tested over the range 9–13 (in l_0 units). With the truncation level adopted here, no significant variation has been observed in the results.

3.2. *Validation of the numerical method*

A thorough validation of the numerical method has been performed in Fontane (2005). We retrieved exactly the two-dimensional stability results of Michalke (1964) for the homogeneous mixing layer and Joly (2002) for its variable-density counterpart. The three-dimensional stability analysis has also been performed for both the Stuart vortices and the KH nonlinear wave. The results are in close agreement with Pierrehumbert & Widnall (1982) and KP91. In figure 3, we present the unstable branches of the KH billows for $Re = 300$ at the time the primary wave climaxes. All the modes identified by KP91 are recovered with an excellent agreement for both the growth rate and temporal frequency (see their figure 13). The higher truncation level used for the present study allows us to find two additional modes not reported in their paper. The first one (◀) corresponds to an oscillatory hyperbolic instability and the second one (◁) is a stationary elliptic mode.

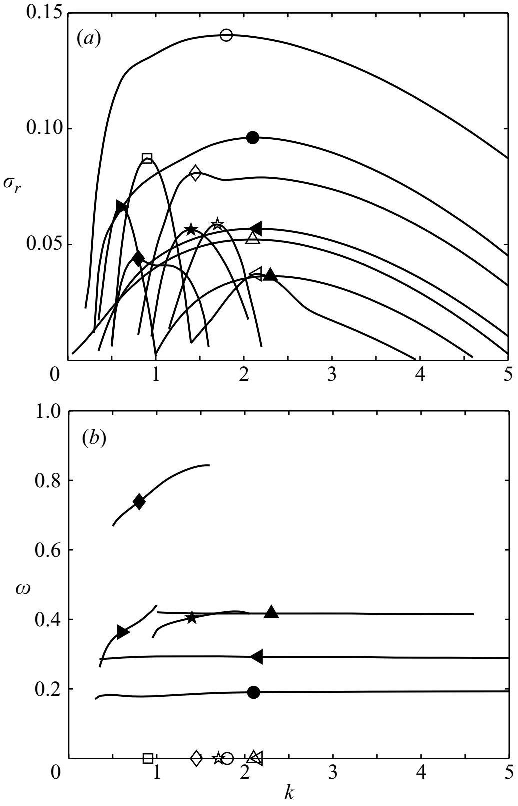

FIGURE 3. (*a*) Growth rate and (*b*) temporal frequency *vs.* spanwise wavenumber k for the maximum-amplitude state ($t = 24$) of the nonlinear KH wave with $C_\rho = 0$ and $Re = 300$. The symbols on each branch denote the fastest growing mode.

4. Secondary instabilities of the variable-density mixing layer

Contrary to shooting methods, stability analyses based on direct methods yield all the eigenmodes available in the frame of a discrete approach. For $N = 55$, the number of eigenvalues in the spectrum rises from $M = 3081$ in the homogeneous case to $M = 4594$ for the variable-density case. Among them, the number of amplified modes is consequent in response to the high Reynolds number and the infinite Schmidt number. Compared to the KP91 case with $Re = 300$, the basic state established with $Re = 1500$ is sensitive to numerous high-wavenumber instabilities as the flow is structured on smaller scales otherwise damped by viscosity. The amplified part of the spectrum is dense and the identification of the unstable branches turns out to be tedious. It relies on the continuity of the growth rate and phase speed with k along the branch. The spatial organization of the eigenmode allows us to discriminate between modes with close eigenvalues and to solve branch crossings in the (k, σ)-plane. In this section, the stability analysis is carried out only at the time the primary Kelvin–Helmholtz wave climaxes, i.e. at $t = 26$. The mean growth rate of the primary wave around the saturation time collapses as shown in table 2. Hence all amplified modes could be retained as they all fulfil the quasi-steady condition (3.6). For the sake of clarity and since only the most unstable modes are likely to emerge in real

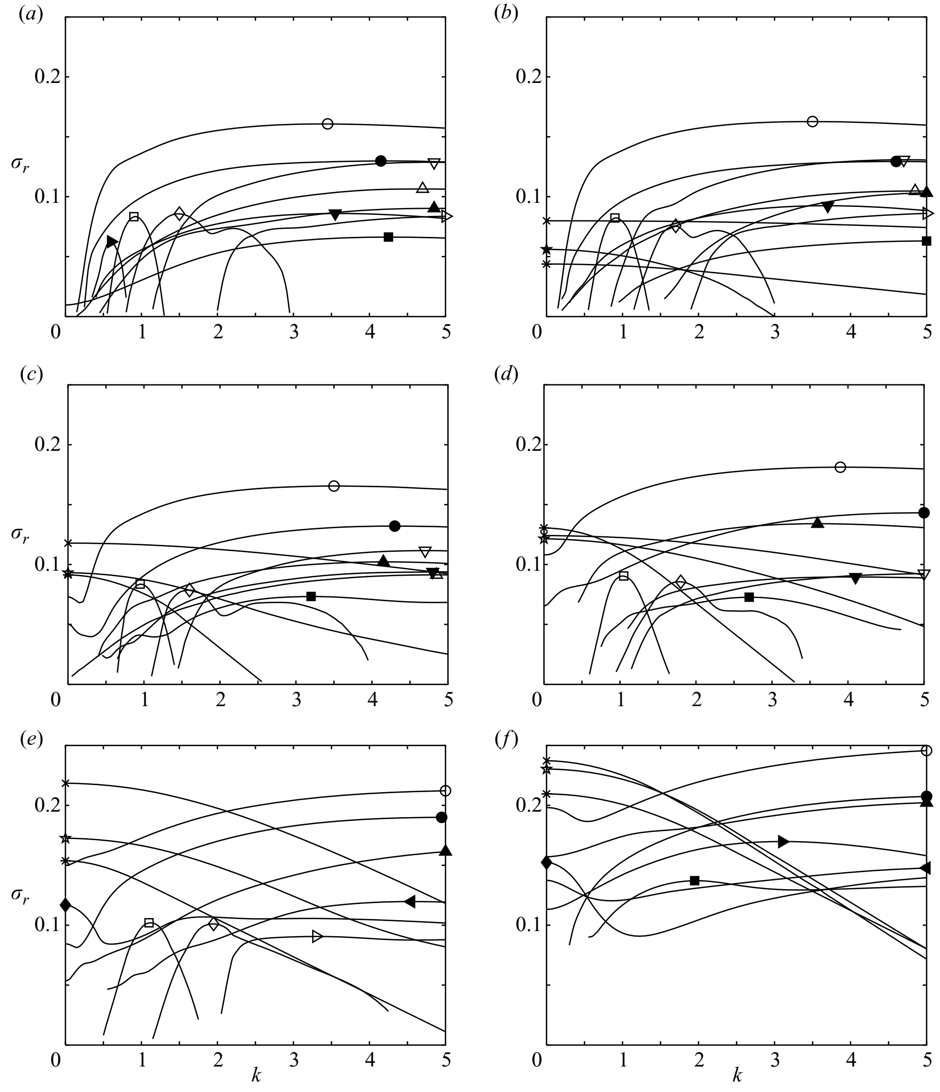

FIGURE 4. Growth rate *vs.* spanwise wavenumber k for the maximum-amplitude state ($t = 26$) of the nonlinear VDKH wave with $Re = 1500$ and various values of the density contrast: (*a*) $C_\rho = 0$, (*b*) $C_\rho = 0.1$, (*c*) $C_\rho = 0.2$, (*d*) $C_\rho = 0.3$, (*e*) $C_\rho = 0.4$ and (*f*) $C_\rho = 0.5$. The symbols on each branch denote the fastest growing mode.

flows, we present the most-amplified modes of each family which reduce to a set of ten principal instabilities.

Figure 4 describes the growth rate versus the spanwise wavenumber for an increasing density contrast. In the homogeneous case, we have a larger Reynolds number than KP91 which results in the spreading of the branches towards higher spanwise wavenumbers (compare figures 4*a* and 3*a*). The increase in Reynolds number favours the growth of hyperbolic modes at high spanwise wavenumbers while the growth rate of elliptic modes remains unchanged. By definition, hyperbolic modes take place in the strained braid region around the saddle point of the streamfunction. Hence they benefit from the development of small length scales and give rise to broadband instabilities. Despite this well-known Reynolds-number effect, we retrieve an unstable spectrum classically divided into core-centred and braid-centred modes. All the branches observed in the homogeneous case and corresponding to these two families will be referred to as homogeneous modes hereinafter.

The variable density Kelvin–Helmholtz billow exhibits biased homogeneous modes and new modes emerging from the specific features of the base flow. We will see further that the latter are two-dimensional shear instabilities of the vorticity braid, but let us analyse first the modifications of the homogeneous or three-dimensional modes.

The growth rate, temporal frequency and peak wavenumber of core-centred modes remain almost unchanged. Their structure is altered as the symmetry breaking of the base flow triggers a growing asymmetry of the eigenmodes. This can be seen in figures 5(*c*, *e*) displaying contours of the kinetic energy per mass unit, $\tilde{k} = |\tilde{u}|^2 + |\tilde{v}|^2 + |\tilde{w}|^2$. This is also true for the hyperbolic mode which concentrates on the thin vorticity ridge at the left of the saddle point (see figures 5*e*, *f*). As described in § 2, the baroclinic vorticity production enhances vorticity and shear on the braid lying on the light side of the VDKH. As such this layer is the best candidate to hold the shear conversion mechanism advocated by KP91 to promote the onset of three-dimensional motions. At $C_\rho = 0.4$, not only is the energy distribution of the stationary hyperbolic mode altered, but also its growth rate and peak spanwise wavenumber. This instability has a larger growth rate, $\sigma_r = 0.215$, and develops on smaller spanwise periods, $k \geqslant 5$, than its symmetric homogeneous counterpart for which $\sigma_r = 0.16$ at $k = 3.5$. For the larger density contrast examined here, $C_\rho = 0.5$, the core-centred elliptic mode does not emerge from the cloud of weakly amplified modes and is not referenced in figure 4(*f*). In the meantime, the hyperbolic mode is overintensified with a growth rate raised to $\sigma_r = 0.246$ for $k = 5$. While the competition between these two kinds of instabilities is balanced in the homogeneous shear layer (Metcalfe *et al.* 1987; Klaassen & Peltier 1991), the present results assert that the hyperbolic modes will prevail over elliptic modes in the variable-density case.

In response to the transformation of the primary roll-up from the smooth homogeneous billow to the layered variable-density structure, a new family of modes emerges in the spectrum. Additional branches appear in figure 4(*b*–*f*) with a maximum growth rate for $k = 0$ denoting a two-dimensional mode. From figure 6, the energy of these modes is found to concentrate in the sharp vorticity ridges of the base flow where the baroclinic vorticity production is most intense. The central isopycnic line of the base flow where $\rho = \rho_0$ is also plotted in order to locate the mode within the VDKH billow. For a small density contrast, the mode is located on the braid end lying on the light side, see figure 6(*a*). For a higher density contrast, the mode is active in two distinct regions, as seen from figure 6(*b*). It still prevails on the lower braid, but also develops inside the light fluid tongue engulfed into the vortex core. Both the vorticity and density fields of these modes, displayed in figure 6(*c*–*f*), consist of an alternation on a short wavelength of sinks and sources along the vorticity sheet. Their wavelength $\lambda_{2\mathrm{D}}$ is estimated as $\lambda_{2\mathrm{D}} \simeq \lambda_x/16$ for $C_\rho = 0.1$ and $\lambda_{2\mathrm{D}} \simeq \lambda_x/11$ for $C_\rho = 0.5$. This perturbation pattern is characteristic of a Kelvin–Helmholtz shear instability. This mode is identical to the secondary baroclinic instability found by Reinaud *et al.* (2000) in their two-dimensional inviscid simulations.

The enhanced vorticity layer can be modelled as a one-dimensional vorticity sheet submitted to a strain field induced by the rolling of the primary wave. The Squire's theorem applied to this model ensures that the most amplified mode is two-dimensional. The present stability analysis is consistent with this simplified model as

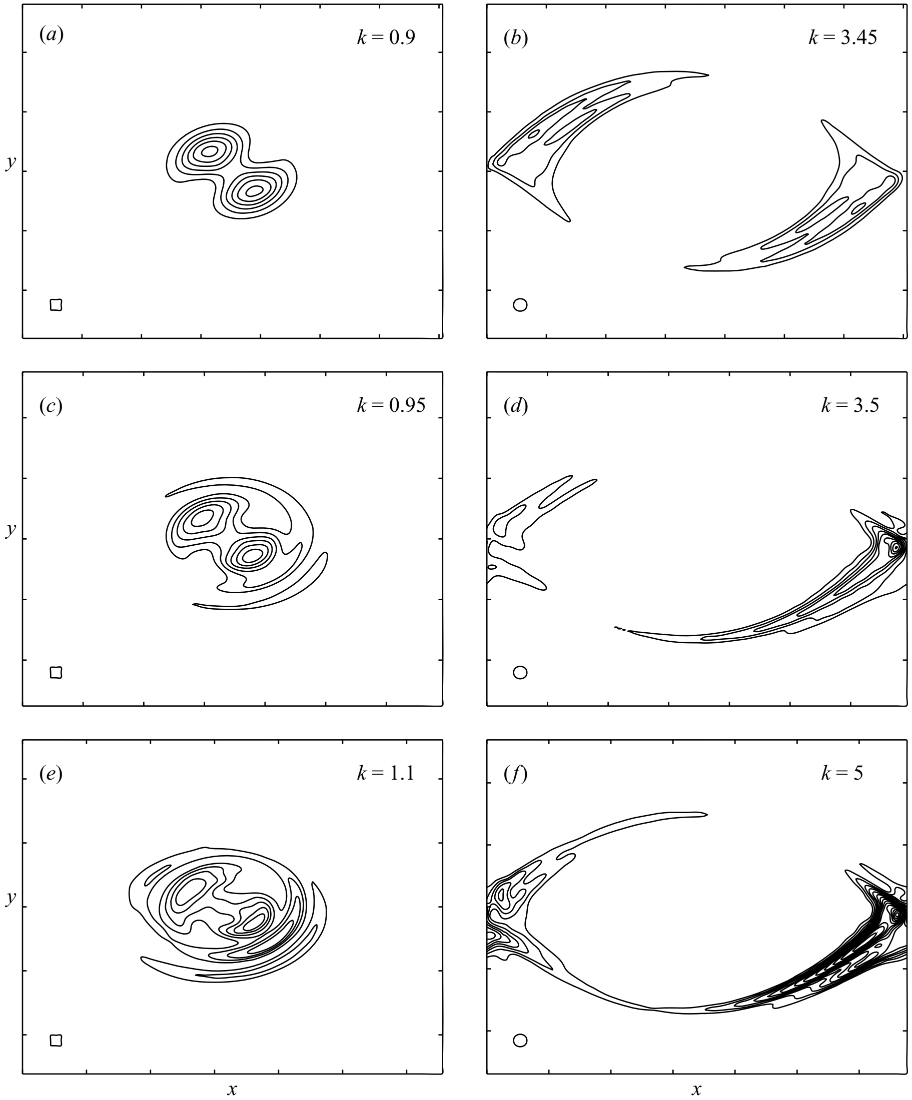

FIGURE 5. Structure of the elliptic mode (□) and the hyperbolic mode (○): iso-levels of energy with (*a*) $C_\rho = 0$, $\sigma_r = 0.083$, (*b*) $C_\rho = 0$, $\sigma_r = 0.161$, (*c*) $C_\rho = 0.2$, $\sigma_r = 0.084$, (*d*) $C_\rho = 0.2$, $\sigma_r = 0.165$, (*e*) $C_\rho = 0.4$, $\sigma_r = 0.102$ and (*f*) $C_\rho = 0.4$, $\sigma_r = 0.212$. Energy is normalized to be unitary and the contour increment is $u_0^2/4$.

the maximum growth rate is found for $k = 0$. The stability of the layer is known to depend on the competition between strain and vorticity. Whereas the vorticity layer alone is unstable, the strain field has a stabilizing effect. Its associated solenoidal velocity field damps oscillations in the direction normal to the sheet and stretches the perturbation wavelengths in the tangential direction, eventually beyond the unstable range. According to this analysis due to Dritschel *et al.* (1991), a strain rate to vorticity ratio γ/Ω above 0.25 prevents the growth of any perturbation. Below this threshold, the linear approach states that the amplification factor increases with decreasing levels of γ/Ω. However, the strain rate to vorticity ratio must be as low as 0.065 to yield

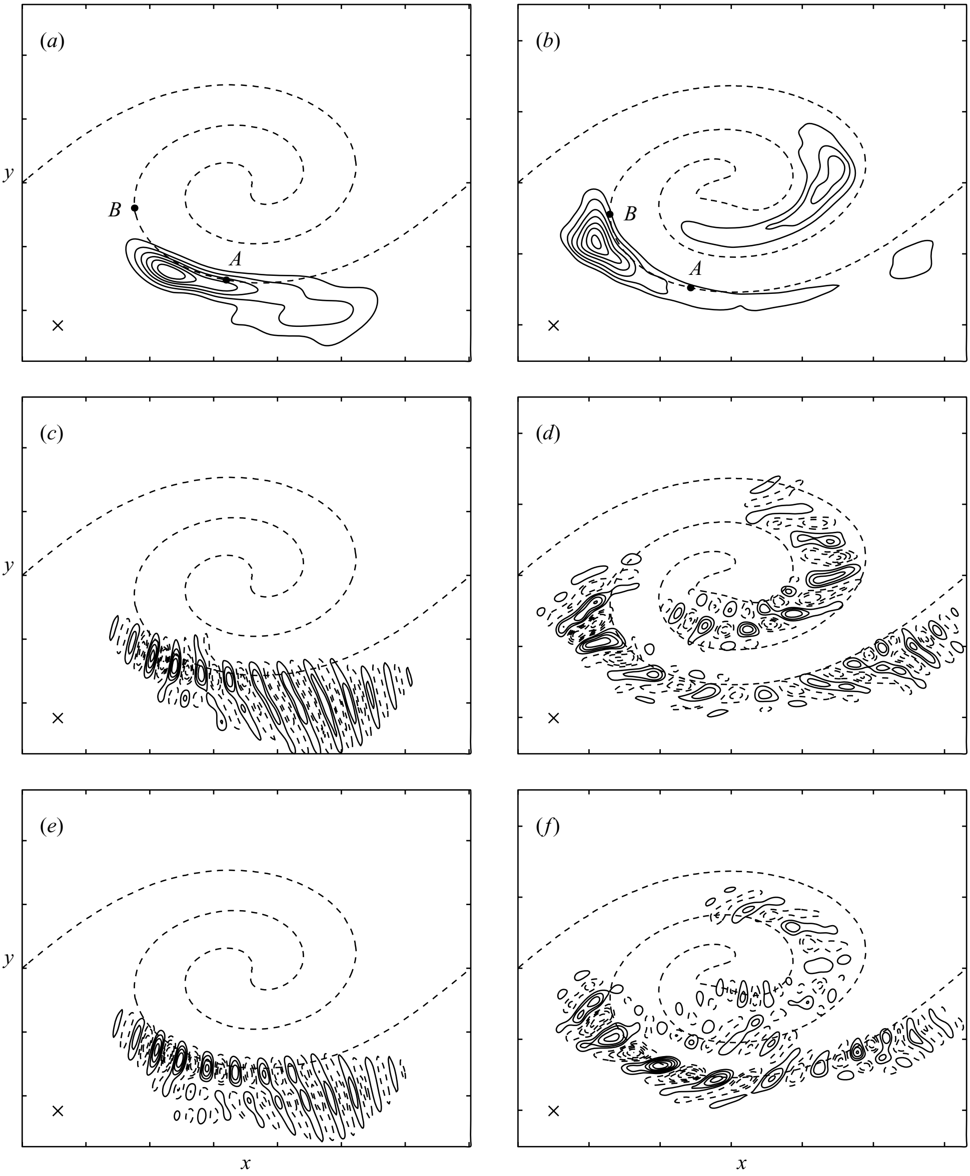

FIGURE 6. Structure of the most amplified two-dimensional baroclinic Kelvin–Helmholtz mode (×) at $C_\rho = 0.1$ (a, c, e) and $C_\rho = 0.5$ (b, d, f). $k = 0$. The contours represent iso-levels of energy in (a) and (b), iso-levels of spanwise vorticity in (c) and (d), iso-levels of density in (e) and (f). The mode characteristics are $\sigma_r = 0.0799$, $\omega = 9.45$ for $C_\rho = 0.1$ and $\sigma_r = 0.237$, $\omega = 4.6$ for $C_\rho = 0.5$. Perturbations are normalized to have a unitary energy. The contour increments are, respectively, $u_0^2/4$, $1/2t_0$ and $\Delta\rho/2$ for the energy, vorticity and density fields. The dashed levels correspond to negative values and the dashed line denotes the central isopycnic line of the base flow. Points A and B are defined in figure 7.

an amplification factor of 3. This particular level of γ/Ω is considered therefore as a convenient threshold for the onset of the shear instability. A similar analysis was transposed by Staquet (1995) and Smyth (2003) to the secondary two-dimensional instability occurring at the saddle point of the stratified mixing layer.

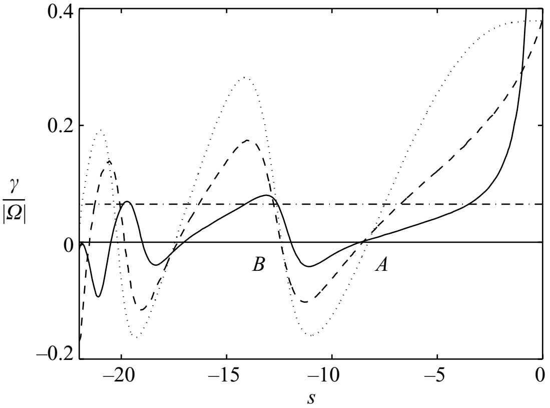

FIGURE 7. Ratio of the strain rate γ to the vorticity Ω along the central isopycnic line. s is the curvilinear coordinate originating at the saddle-point, approximated here as the point of maximum γ. …, $C_\rho = 0$; — — —, $C_\rho = 0.1$; —, $C_\rho = 0.5$. The dashed-dotted line denotes a threshold value of 0.065 and A, B represent the first positions with zero strain rate starting from the saddle point.

We measure the strain rate along the central isopycnic line by $\gamma = \boldsymbol{\eta} \cdot \nabla \boldsymbol{u} \cdot \boldsymbol{\eta}$ where $\boldsymbol{\eta}$ is a unit vector normal to the density gradient. From figure 7 it is seen that, in the variable-density case, any arbitrary threshold of $\gamma/|\Omega|$ is reached closer to the saddle point where the stretching rate is maximum. This argument was first invoked by Reinaud *et al.* (2000) in their analysis of the basic mechanism leading to the baroclinic secondary instability. The portion of the negative vorticity braid where $\gamma/|\Omega| \leqslant 0.065$ presents a wider extent as the density contrast is increased. Consistently, the perturbation spreads over a longer part of the braid, as can be seen in figure 6. Between points A and B where the strain collapses, the vorticity layer is submitted to a compression strain field favourable to the growth of the instability. It is not surprising then that the energy of the perturbation peaks between A and B. In the homogeneous case, the compression zone is part of the core and is beyond the scope of the vorticity-sheet model.

We thus retrieved the secondary baroclinic instability of Reinaud *et al.* (2000) from a direct linear stability analysis of the base flow rather than from inviscid numerical simulations. These new results assert the relevancy of the mechanism to the transition of high-Reynolds-number variable-density mixing layers without mass diffusion. The instability being of Kelvin–Helmholtz type, its onset is not precluded by momentum diffusion, i.e. finite Reynolds number. In contrast Reinaud *et al.* (2000) we are able to discuss the competition with three-dimensional modes and with the pairing mode. To answer the latter point, we performed a stability analysis varying the Floquet exponent μ from 0 to unity, as was done by Pierrehumbert & Widnall (1982) and Klaassen & Peltier (1989) for the Stuart vortices and the stratified mixing layer. In particular, we focused on the two-dimensional subharmonic modes, $\mu = 0.5$, for the most density-contrasted case, $C_\rho = 0.5$. From the contours of their vorticity fields (not displayed here), the most amplified subharmonic modes are identified as shear instabilities of the vorticity braid in phase opposition between two consecutive VDKH billows. The most amplified subharmonic mode has a growth rate of $\sigma_r = 0.227$ to be compared to $\sigma_r = 0.237$ for the shear instability on a single period, i.e. with $\mu = 0$. Hence we switch from the concurrent growth between three-dimensional modes and

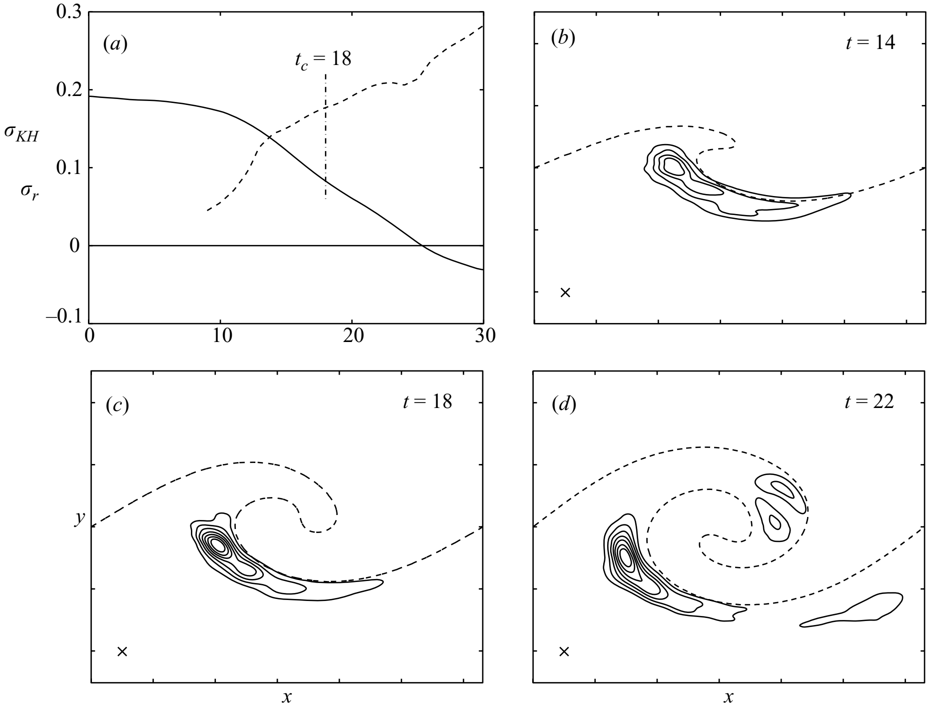

FIGURE 8. (*a*) Temporal evolution of the growth rates of both the VDKH billow (solid line) and the secondary shear instability (dashed line) for $C_\rho = 0.5$. The vertical line denotes the critical time $t_c = 18$. Energy contours of the two-dimensional mode for (*b*) $t = 14$, (*c*) $t = 18$ and (*d*) $t = 22$ with $u_0^2/4$ as contour increment.

the two-dimensional pairing mode in the homogeneous mixing layer, to a variable-density mixing layer where the enhanced vorticity braid fed by baroclinic vorticity redistribution is the location where a secondary two-dimensional shear instability may compete with the growth of shear conversion to three-dimensional motions.

5. Nonlinear development of the secondary two-dimensional mode

In the previous section, the results of the stability analysis are examined at $t = 26$. We now focus on the two-dimensional mode and check its persistence along the development of the primary VDKH-wave. For $C_\rho = 0.5$, figure 8(*a*) compares the temporal evolution of its growth rate with that of the primary instability. The mode is already present in the spectrum around $t = 10$, though weakly unstable. It is not likely to develop at this stage since the low value of σ_r violates the quasi-steady assumption. Following KP91, we conventionally define the critical time t_c at which the growth rate of the two-dimensional mode first exceeds twice the growth rate of the primary wave, i.e. $\sigma_r \geqslant 2\sigma_{KH}$. From the critical time, $t_c = 18$, the relevancy of the two-dimensional mode is verified.

From the energy contours of figure 8(*b*–*d*), we identify the two-dimensional mode from its main feature – the energy peaks in the compression zone below the central isopycnic line. The vorticity and density perturbations are organized into alternate sources and sinks, similar to those displayed at $t = 26$ in figure 6(*d*, *f*). The second spot of energy in the right-hand part of the core, displayed in figure 6(*b*) at $t = 26$, emerges around $t = 22$ as can be seen in figure 8(*d*). For early times, $t \lesssim 20$, the primary wave has not overturned yet and the core of the VDKH billow has not developed into a coiled vorticity sheet.

We now illustrate the nonlinear development of the least-stable two-dimensional mode based on the numerical continuation of a perturbed VDKH wave. In agreement with the previous discussion, we seed the most density-contrasted variable-density KH-wave at the critical time $t_c = 18$ with the perturbation issuing from the stability analysis performed at the same time. The perturbation is given an amplitude such that its enstrophy is 0.6 % of the enstrophy of the base flow over the period. The same scaling factor is applied to both the velocity and density perturbation fields. The adaptive spatial resolution based on the condition $\min(\eta_\rho) > 3\Delta$ leads to a final 8064^2 grid at $t = 28$. This highly demanding resolution is due to the increased stretching of the material lines by the secondary mode, as will be illustrated later. A pseudospectral code based on a uniform grid is obviously not an optimal choice for this flow where density and velocity gradients concentrate on a small portion of the calculation domain. At least the adaptive time step and spectral radius avoid propagating the spatio-temporal resolution of the final time steps back to the earlier ones.

From figure 9, we see that the perturbation initiates secondary roll-ups in the favoured part of the braid. The alternate vorticity sources and sinks are advected towards the centre of the domain as the primary roll-up proceeds. Since the forcing is performed at $t = 18$ only, no perturbations are applied in the wake of the advected secondary cores. There, the stretched vorticity layer remains stable from the saddle point to the last forming structure. Contrary to the inviscid Lagrangian code used by Reinaud *et al.* (2000) which spontaneously revealed and sustained the two-dimensional instability, the present fully resolved (low-noise) pseudospectral simulations at finite Reynolds number are too smooth to excite it continuously. The breakup of the vorticity braid is completed by $t = 24$ and newly formed secondary structures present the same organization as the VDKH billow. The acceleration pattern around the saddle point of the primary wave repeats itself at this smaller scale. The baroclinic torque produces negative vorticity on the light side and positive vorticity on the heavy one, leading to the concentration of vorticity on comma-shaped layers. As was pointed out by Reinaud *et al.* (2000), this is typical of a two-dimensional cascade towards smaller scales presenting the features of a fractal process with scale invariance of the flow structure. If not limited by momentum diffusion and calculation cost, we eventually witness the breakup of the secondary vorticity braids into third-generation small-scale billows. This is illustrated in Fontane *et al.* (2008) where the perturbation is injected earlier at $t = 13$. In real flows, we expect this third generation to be prevented by the prior rise of three-dimensionality.

Corresponding density contours illustrating the growing complexity of the scalar field are shown in figure 10. Light fluid (white) and heavy fluid (grey) are seen to intermingle on small scales in response to the secondary roll-ups. A large impact on the mixing rate is expected. We thus measure the increase of the interfacial area between the two fluids from the stretching of the central isopycnic line. The time evolution of its length, denoted ℓ_{cil}, is plotted on a logarithmic scale in figure 11 where the perturbed and unperturbed flows are compared. From $t = 12$, the primary wave alone triggers an exponential growth $\ell_{cil} \sim \exp(\sigma_\ell t)$ with $\sigma_\ell = 0.085$, nearly half the value of the primary mode growth rate (see table 1). The onset of the two-dimensional secondary mode from $t = 18$ raises the ℓ_{cil}-growth rate up to $\sigma_\ell = 0.24$, close to $\sigma_r = 0.237$ as measured by the stability analysis. This latter

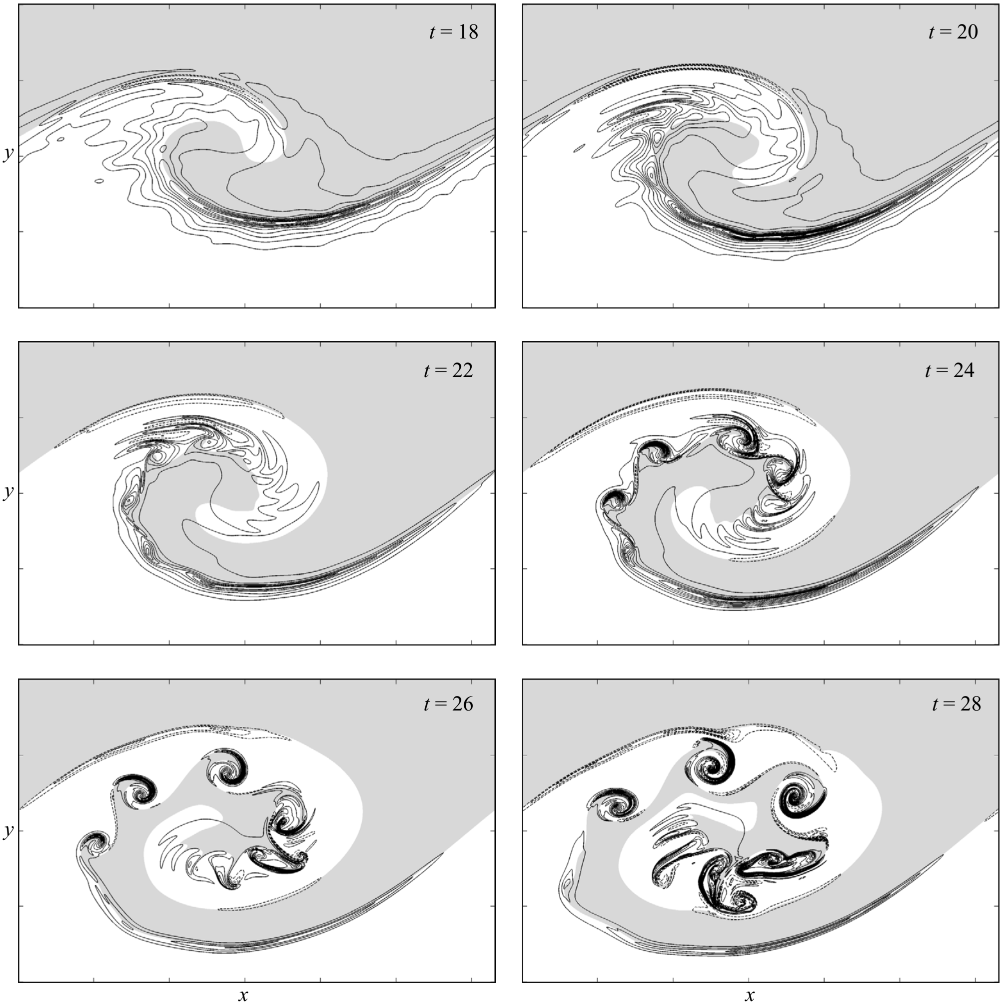

FIGURE 9. Vorticity contours of the temporally evolving mixing layer $C_\rho = 0.5$ seeded at $t = 18$ with the two-dimensional perturbation of the favoured vorticity braid. The vorticity increment between contours is $1/4t_0$ at $t = 18, 20$, $1/2t_0$ at $t = 22, 24$ and $1/2t_0$ at $t = 26, 28$. Positive contours are drawn with dashed lines. The grey-shaded region corresponds to the domain where the density is higher than ρ_0. Tick marks along x and y axes are separated by the initial vorticity thickness $\delta_\omega^0 = 2l_0$.

agreement between σ_ℓ and σ_r should be considered as pure coincidence – note their difference in the case with no perturbation of the secondary mode. The central isopycnic line experiences a time-evolving strain field of alternate stretchings and compressions between consecutive hyperbolic regions. We measure here only the result of this complex history. Commenting on the simpler situation described by Corcos & Sherman (1984), Ottino (1989) stressed that, within an homogeneous KH-billow, the details of the stretching history of fluid elements are highly complicated. In the VDKH-billow submitted to the secondary baroclinic instability, both the primary and secondary roll-ups contribute to the folding of the material lines. Besides, the small-scale wrapping of the material interface is only active on the perturbed fraction of the central line. Indeed, no quantitative relationship emerges between the growth

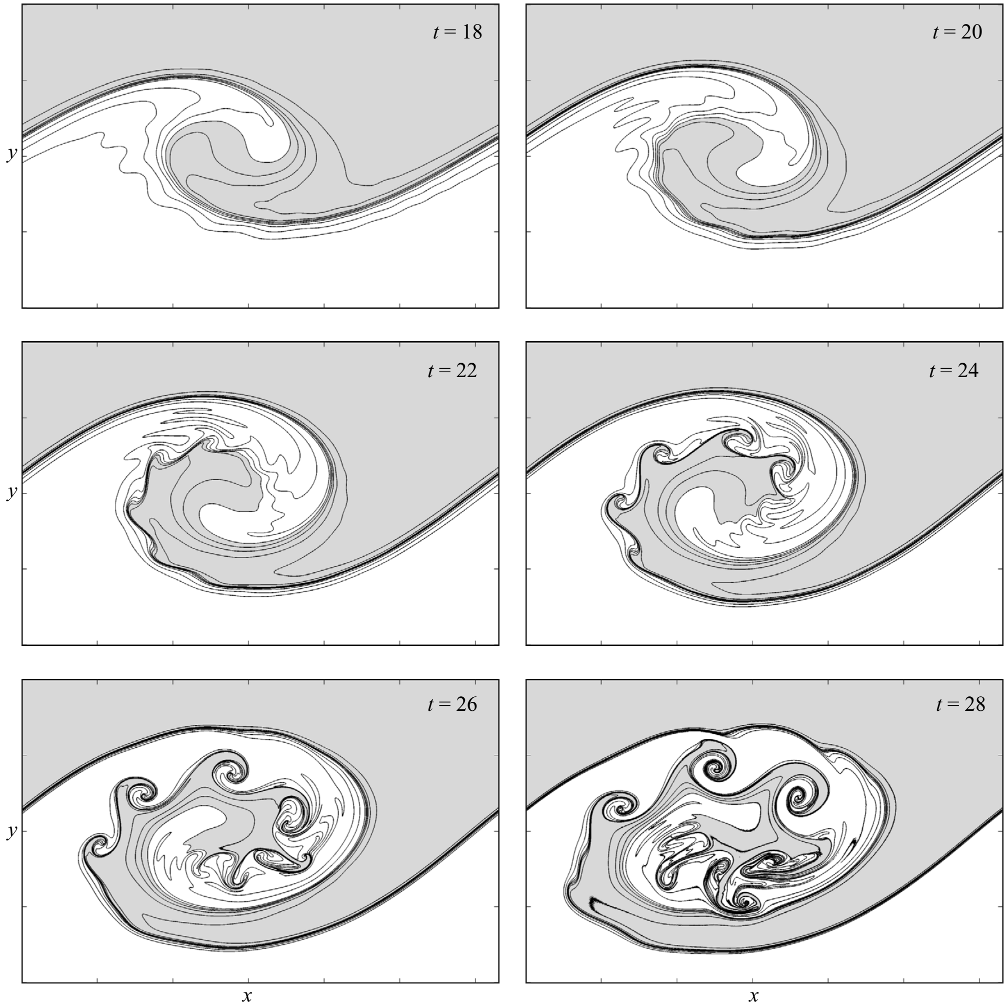

FIGURE 10. Density contours of the temporally evolving mixing layer $C_\rho = 0.5$ seeded at $t = 18$ with the two-dimensional perturbation of the favoured vorticity braid. The density increment between contours is $\Delta\rho/10$. The grey-shaded region and tick marks are defined as in figure 9.

of the kinetic energy perturbations of the and their by-product in terms of stretching integrated along one particular material line.

From the stability analysis, we found numerous two-dimensional secondary modes less amplified than the one selected here. Some of them focused elsewhere on the vorticity braid, for example on the heavy fluid side supplied with positive vorticity. A superposition of several modes would have triggered secondary roll-ups on a larger portion of the central isopycnic line. Though unlikely to happen naturally, such a complex modal perturbation would yield even larger exponential growth of the interfacial length. Finally, the two-dimensional secondary shear-instability of stretched layers of vorticity and density-gradient, comes out as a good candidate for promoting mixing, together with more standard transition mechanisms appealing to three-dimensionalization.

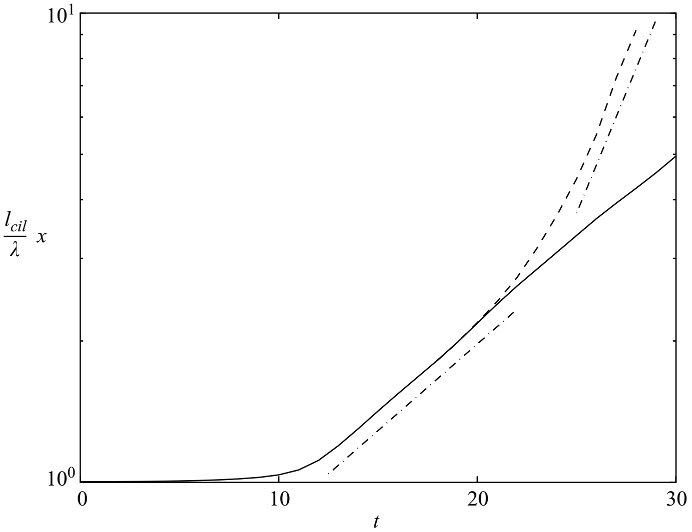

FIGURE 11. Temporal evolution of the length ℓ_{cil} of the central isopycnic line normalized by λ_x. The dashed and solid lines correspond, respectively, to the case with and without the baroclinic secondary instability. The dashed-dotted lines measure respective exponential growth rates $\sigma_\ell = 0.24$ and $\sigma_\ell = 0.085$.

6. Conclusions

In this paper, we address the three-dimensional stability of the mixing layer developing between two fluids of different density. Numerical simulations are carried out to obtain the temporal evolution of the two-dimensional variable-density Kelvin–Helmholtz billows. The Reynolds number is 1500 while both the Schmidt and Froude numbers are infinite. The density contrast is varied between $C_\rho = 0$ and $C_\rho = 0.5$, increasing the intensity of the baroclinic torque and the asymmetric concentration of vorticity onto thin and folded layers. These flow maps are then probed against three-dimensional modes at the saturation time of the primary mode.

The eigenmodes issued from the stability analysis fall into two main classes. In the first class, we find the elliptic and hyperbolic modes already identified by KP91 in the homogeneous mixing layer. Because of baroclinic redistribution, the braid region evolves in sharp vorticity ridges and holds high shear and strain rates favourable to the development of secondary instabilities. The growth rate of hyperbolic modes increases with the density contrast and they develop preferentially on the vorticity-enhanced part of the braid. Hence, elliptic modes, whose growth rate is quite insensitive to changes in the base flow, gradually cease from being relevant.

Specific transverse modes form a second class with a maximum growth rate at zero spanwise wavenumber. They refer to a two-dimensional shear instability of the vorticity-enhanced braid, first detected and analysed by Reinaud *et al.* (2000) from inviscid Lagrangian simulations. Beyond the cross-validation of their results, we prove that this secondary instability is also amplified for finite Reynolds number. The perturbation consists in a succession of alternate vorticity sources and sinks associated with a similar density pattern. A further analysis of the strain along the central isopycnic line yields that the perturbation energy peaks in the compression zone first met from the saddle point. The present three-dimensional stability analysis proves that the two-dimensional secondary instability competes fairly with the three-dimensional braid-centred modes at least for $C_\rho \geqslant 0.2$ at saturation time. The vorticity-enhanced braid is thus the unique and preferred location for the development of secondary instabilities in contrast with the homogeneous shear layer where core-centred modes play a significant role.

We perform a fully resolved numerical continuation of the nonlinear development of the two-dimensional mode. The perturbations are seen to trigger a KH-instability of the curved part of the vorticity-enhanced braid which breaks into secondary rollers. As their strength increases, the small-scale roll-ups turn into comma-shaped vorticity layers owing to a baroclinic torque pattern similar to the one biasing the primary KH-billow. We measure a sharp increase in the mixing rate in response to the onset of the two-dimensional mode. In this particular case, the exponential growth rate of the interfacial length raises by a factor of three. More generally, this instability turns out probably to participate in the mixing transition together with three-dimensional modes.

The selection of the secondary instabilities has been discussed for the variable-density mixing layer with no mass diffusion. This approach is justified in itself in order to obtain the most biased response in contrast to the homogeneous flow. However, it precludes carrying out three-dimensional simulations down to the length scale of the non-miscible scalar field. For an infinite Schmidt number, the density gradient and the corresponding vorticity source peak on shear layers thinning unboundedly. In contrast with this situation, monophase binary mixing gaseous flows of practical interest develop under finite-Schmidt-number conditions. The effect of non-zero mass diffusion on the competition between secondary modes must also be addressed. With the diffusive terms in the continuity equation for both the generation of the base flow maps and the stability analysis, we expect to find a simpler spectrum on a smoother base flow. This context will not only allow the discussion of the finite-Schmidt-number effect, but also alleviate the computational cost of three-dimensional simulations including the hyperbolic mode.

In § 5, we superimposed an eigenmode perturbation of the background flow taken at $t_c = 18$. Though close to saturation, the primary roll-up still induces an unsteady advection field that is beyond the scope of our local instability analysis. The least stable eigenmode does not anticipate the flow history from $t_c = 18$ down to a time horizon where the energy of the secondary mode and the induced mixing would be maximized. This requires a different approach of the stability problem better suited for unsteady base flows. We consider the direct-adjoint method, see Schmid (2007), adapted to find the perturbation maximizing the response for a given injection time.

We acknowledge fruitful discussions with Dr Jean N. Reinaud and express our thanks for his helpful comments on the draft of this paper.

REFERENCES

Ashurst, W. T. & Meiburg, E. 1988 Three-dimensional shear layers via vortex dynamics. *J. Fluid Mech.* **189**, 87–116.

Bernal, L. P. & Roshko, A. 1986 Streamwise vortex structures in plane mixing layers. *J. Fluid Mech.* **170**, 499–525.

Brown, G. L. & Roshko, A. 1974 On density and large structure in turbulent mixing layers. *J. Fluid Mech.* **64**, 775–823.

Corcos, G. M. & Lin, S. J. 1984 The mixing layer: deterministic models of a turbulent flow. Part 2. The origin of three-dimensional motion. *J. Fluid Mech.* **139**, 67–95.

CORCOS, G. M. & SHERMAN, F. S. 1984 The mixing layer: deterministic models of a turbulent flow. Part 1. Introduction and the two-dimensional flow. *J. Fluid Mech.* **139**, 29–65.

CORTESI, A. B., YADIGAROGLU, G. & BANERJEE, S. 1998 Numerical investigation of the formation of three-dimensional structures in stably-stratified mixing layers. *Phys. Fluids* **10** (6), 1449–1473.

DRITSCHEL, D. G., HAYNES, P. H., JUCKES, M. N. & SHEPHERD, T. G. 1991 The stability of a two-dimensional vorticity filament under uniform strain. *J. Fluid Mech.* **230**, 647–665.

FONTANE, J. 2005 Transition des écoulements cisaillés libres à densité variable. PhD thesis, Institut National Polytechnique de Toulouse.

FONTANE, J., JOLY, L. & REINAUD, J. N. 2008 Fractal Kelvin–Helmholtz break-ups. *Phys. Fluids, Gallery of Fluid Motion* (to be published).

JIMENEZ, J. 1983 A spanwise structure in the plane shear layer. *J. Fluid Mech.* **132**, 319–336.

JOLY, L. 2002 Inertia effects in variable density flows. Habilitation à Diriger des Recherches INPT.

JOLY, L. & REINAUD, J. N. 2007 The merger of two-dimensional radially stratified high-Froude-number vortices. *J. Fluid Mech.* **582**, 133–151.

JOLY, L., REINAUD, J. N. & CHASSAING, P. 2001 The baroclinic forcing of the shear layer three-dimensional instability. *2nd Intl Symp. on Turbulence and Shear Flow Phenomena, Stockholm* vol. 3, pp. 59–64.

JOLY, L., FONTANE, J. & CHASSAING, P. 2005 The Rayleigh–Taylor instability of two-dimensional high-density vortices. *J. Fluid Mech.* **537**, 415–431.

JOSEPH, D. 1990 Fluid dynamics of two miscible liquids with diffusion and gradient stresses. *Eur. J. Mech.* B/*Fluids* **9**, 565–596.

KLAASSEN, G. P. & PELTIER, W. R. 1985 The onset of turbulence in finite-amplitude Kelvin–Helmholtz billows. *J. Fluid Mech.* **155**, 1–35.

KLAASSEN, G. P. & PELTIER, W. R. 1989 The role of transverse secondary instabilities in the evolution of free shear layers. *J. Fluid Mech.* **202**, 367–402.

KLAASSEN, G. P. & PELTIER, W. R. 1991 The influence of stratification on secondary instability in free shear layers. *J. Fluid Mech.* **227**, 71–106.

KNIO, O. M. & GHONIEM, A. F. 1992 The three-dimensional structure of periodic vorticity layers under non-symmetric conditions. *J. Fluid Mech.* **243**, 353–392.

LASHERAS, J. C. & CHOI, H. 1988 Three-dimensional instability of a plane free shear layer: an experimental study of the formation and evolution of streamwise vortices. *J. Fluid Mech.* **189**, 53–86.

LASHERAS, J. C., CHO, J. S. & MAXWORTHY, T. 1986 On the origin and evolution of streamwise vortical structures in a plane, free shear layer. *J. Fluid Mech.* **172**, 231–258.

LEBLANC, S. & CAMBON, C. 1998 Effects of Coriolis force on the stability of Stuart vortices. *J. Fluid Mech.* **356**, 353–379.

MAYER, E. W. & POWELL, K. G. 1992 Viscous and inviscid instabilities of a trailing vortex. *J. Fluid Mech.* **245**, 207–243.

METCALFE, R. W., ORSZAG, S. A., BRACHET, M. E., MENON, S. & RILEY, J. J. 1987 Secondary instability of a temporally growing mixing layer. *J. Fluid Mech.* **184**, 207–243.

MICHALKE, A. 1964 On the inviscid stability of the hyperbolic-tangent velocity profile. *J. Fluid Mech.* **19**, 543–556.

NYGAARD, K. J. & GLEZER, A. 1990 Core instability of the spanwise vortices in a plane mixing layer. *Phys. Fluids* A **2** (3), 461–464.

O'REILLY, G. & PULLIN, D. I. 2003 Structure and stability of the compressible Stuart vortex. *J. Fluid Mech.* **493**, 231–254.

OTTINO, J. M. 1989 *The Kinematics of Mixing: Stretching, Chaos and Transport*. Cambridge University Press.

PIERREHUMBERT, R. T. & WIDNALL, S. E. 1982 The two- and three-dimensional instabilities of a spatially periodic shear layer. *J. Fluid Mech.* **144**, 59–82.

REINAUD, J., JOLY, L. & CHASSAING, P. 2000 The baroclinic secondary instability of the two-dimensional shear layer. *Phys. Fluids* **12** (10), 2489–2505.

ROGERS, M. M. & MOSER, R. D. 1992 The three-dimensional evolution of a plane mixing layer: the Kelvin–Helmholtz rollup. *J. Fluid Mech.* **243**, 183–226.

SCHMID, P. J. 2007 Nonmodal stability theory. *Annu. Rev. Fluid Mech.* **39**, 129–162.

Schowalter, D. G., Van Atta, C. W. & Lasheras, J. C. 1994 A study of streamwise vortex structure in a stratified shear layer. *J. Fluid Mech.* **281**, 247–292.

Smyth, W. D. 2003 Secondary Kelvin–Helmholtz instability in weakly stratified shear flow. *J. Fluid Mech.* **497**, 67–98.

Soteriou, M. C. & Ghoniem, A. F. 1995 Effect of the free-stream density ratio on free and forced spatially developing shear layers. *Phys. Fluids* A **7** (8), 2036–2051.

Staquet, C. 1995 Two-dimesnional secondary instabilities in a strongly stratified shear layer. *J. Fluid Mech.* **296**, 73–126.